Engineering Science and Technology, an International Journal 56 (2024) 101779

Contents lists available at ScienceDirect

Engineering Science and Technology,
an International Journal

journal homepage: www.elsevier.com/locate/jestch

Full Length Article

Advanced sensor for non-invasive breast cancer and brain cancer diagnosis using antenna array with metamaterial-based AMC

Musa N. Hamza [a,*], Mohammad Tariqul Islam [b,*], Slawomir Koziel [c,d]

[a] Department of Physics, College of Science, University of Raparin, Sulaymaniyah 46012, Iraq
[b] Department of Electrical, Electronic and Systems Engineering, Faculty of Engineering and Built Environment, Universiti Kebangsaan Malaysia, 43600 UKM Bangi, Selangor, Malaysia
[c] Engineering Optimization & Modeling Center, Reykjavik University, 102 Reykjavik, Iceland
[d] Faculty of Electronics, Telecommunications and Informatics, Gdansk University of Technology, 80-233 Gdansk, Poland

ARTICLE INFO

Keywords:
Artificial magnetic conductor (AMC)
Early-stage breast and brain tumor detection
Microwave imaging (MWI)
Biosensors
Broadband antennas
Gain enhancement
Metamaterials (MTMs)

ABSTRACT

Microwave imaging techniques can identify abnormal cells in early development stages. This study introduces a microstrip patch antenna coupled with artificial magnetic conductor (AMC) to realize improved sensor for non-invasive (early-stage) breast cancer and brain cancer diagnosis. The frequency selectivity of the proposed antenna has been increased by the presence of AMC by creating an additional resonance at 2.276 GHz associated with peak gain of 8.15 dBi and 10.02 dBi, with and without AMC, respectively. High precision and high-quality imaging in the field of medical diagnostics are ensured by the directive radiation pattern of the sensor, emitted from the center of the sensor's front surface. The antenna has been manufactured and experimentally validated with measurement results being in good agreement with the full-wave simulations. In particular, the measured broadside gain at the operating frequency is 11.7 dBi. The presented structure has been incorporated in the microwave imaging system for breast and brain cancer identification. Extensive simulation studies corroborate its suitability for the task based on the analysis of multiple scenarios of tumor detection. Furthermore, our antenna has been favorably compared to state-of-the-art designs reported in the literature showing its competitive performance, especially in terms of size, impedance matching bandwidth, and gain trade-offs.

1. Introduction

Breast cancer is caused by gene mutations, resulting in irregular growth and tumor formation that can spread to other areas of the body [1,2]. Breast cancer is the most common malignancy among women [1,2], projected to increase from 14 million to 22 million in the next 20 years [3]. Early diagnosis is the most successful method of treating breast cancer [4], with a 99 % survival rate [5]. Brain-related illnesses, such as brain tumors, place a strain on people and the healthcare system, leading to severe mortality and shortening life expectancy. They are the ninth-greatest cause of death worldwide. There are two forms of brain tumors: benign and malignant. Global brain tumor cases have been rising rapidly: 88,970 US patients were diagnosed in 2022. Benign tumors have a homogeneous structure and regular shape, whereas malignant tumors have a heterogeneous structure and irregular shape. They grow slowly, while malignant tumors grow uncontrollably. Early detection, monitoring, and proper investigation can reduce deaths and increase survival rates.

The most popular methods for breast cancer detection include mammography, MRI, and ultrasound [6,7]. Mammography has led to incorrect diagnoses and outcomes, affecting the patient life quality [4], and deterring women from regular checkups due to X-rays and discomfort [8–10]. MRI is sensitive to dense breasts but inaccurately diagnoses them due to breast instability during scanning [8,9,11]. Poor ultrasound imaging makes it difficult to distinguish cancerous cells from healthy ones [4,8,10]. Brain tumors are also diagnosed using a variety of imaging techniques, including CT scanning, X-ray screening, MRI, biopsy, PET, and ultrasound screening. The disadvantages of these technologies include increased cancer risk, high radiation doses, high ionizing radiation, high costs, risk to patients with pacemakers and implanted cardioverter devices, time commitment, and decreased susceptibility. The cost-effectiveness, non-ionizing, non-invasive, risk-free, low-powered penetration, and safety aspects of microwave imaging research are attracting interest for medical applications.

---

* Corresponding authors.
E-mail addresses: musa.nuraden@uor.edu.krd (M.N. Hamza), tariqul@ukm.edu.my (M.T. Islam).

https://doi.org/10.1016/j.jestch.2024.101779
Received 12 September 2023; Received in revised form 14 July 2024; Accepted 15 July 2024

In contrast to these methods, microwave imaging (MWI) offers low cost, accuracy, non-ionizing nature, and comfortable placement [12]. Microwave Imaging (MWI) is an emerging technology with promising potential for non-invasive cancer diagnosis. While MWI is not yet a standard clinical tool, ongoing research and development efforts are focused on improving its accuracy, reliability, and user-friendliness. Clinical trials are underway to evaluate its efficacy for cancer detection in various settings. MWI leverages alteration of the backscattered signal by changes in the electrical properties of tissues, specifically, their dielectrical features [7–9]. By analyzing the electromagnetic wave scattering patterns, MWI detects changes in the electrical characteristics of tissues, such as permittivity and conductivity, that may indicate the presence of malignant cells. Typically, low-power microwaves are employed [13–15]. The waves are directed at the body, and their reflections are acquired by a receiving network of antennas. MWI can identify and categorize different forms of cancer by comparing these measures to a database of known patterns. Furthermore, because MWI is non-invasive and does not use hazardous radiation, it is a safer option than conventional detection methods [4,6,16–19]. One of the key components of MWI setups are antennas, utilized to produce electromagnetic fields propagating through the tissue under investigation. As mentioned earlier, the analysis of the scattering patterns allows for identifying suspicious changes such as tumors due to their abnormal dielectric properties. The most important performance parameters of antenna structures used in the context of MWI are gain, radiation pattern, and impedance bandwidth. These factors determine the MWI system's sensitivity and accuracy in identifying and categorizing malignant cells. Furthermore, the size and form of the antenna structure are important in improving the signal-to-noise ratio and limiting interference for accurate measurements.

A number of studies have been conducted on the subject of detecting breast and brain cancer, which employ a variety of microwave imaging equipment. The antenna solutions investigated for breast cancer detection include side-slotted Vivaldi antenna[12], CPW-fed EBG-based antenna [9], rectangular slotted patch antenna [20], antipodal Vivaldi antenna [21], slotted antipodal Vivaldi antenna [22], antipodal Vivaldi antenna [18], side slotted Vivaldi antenna [23], CPW-fed monopole antenna [24], or semi-circle shaped planar antenna [8]. Antenna structures developed for brain cancer identification include, among others, a cross-fed 3D slot-loaded antenna [25], EBG-based microstrip patch [26], GCPW- based slotted inverted delta shaped patch [27], antipodal Vivaldi antenna [28], metamaterial-loaded stacked antenna array [29], conformal wideband antenna [30], bowtie antenna [31], wideband monopole antenna [32], 3D stacked folded antenna [33], 3D-slot-loaded folded dipole [34], or 3D stacked wideband antenna [35]. The analysis of the existing literature indicates that only bandwidth optimization has been taken into account for the majority of reported designs. Other characteristics, such as gain and radiation properties, have received less attention. Nonetheless, the operation and performance of MWI is contingent upon all three. Furthermore, all of the systems discussed in the literature were designed to identify a single form of cancer. Whereas, sensor that exhibit enhanced gain, appropriate radiation pattern, and bandwidth might be used to create reliable, high-resolution screening devices that health professionals can rely on. These sort of devices are needed to detect more than one type of cancer at an early stage.

Our proposed microstrip patch antenna, integrated with an artificial magnetic conductor (AMC), is specifically designed for non-invasive early-stage breast and brain cancer diagnosis. This design aims to enhance frequency selectivity and gain, resulting in high-precision medical imaging. In contrast, the cited works present MIMO antenna designs with varying objectives and methodologies. For instance, one study introduces a compact MIMO antenna with wideband gain enhancement for FMCW radar sensors used in human respiratory monitoring. This design employs a Y-shaped power divider and metasurface to improve radiation patterns and reduce backward radiation, achieving a gain of up to 10.6 dBi and a radiation efficiency between 88.01 % and 90.02 % [36]. Another study features a high-isolation Fabry–Pérot antenna array for Ku-band vehicle satellite communications, utilizing tandem circular parasitic patches and a radial gradient partially reflective surface to achieve a realized gain of up to 21.59 dBi and over 40.8 dB isolation [37]. Additionally, a dual-polarized wideband MIMO antenna for microbase stations incorporates bowtie dipole radiators and parasitic elements, achieving gains of 9.4–11.2 dBi and high isolation with an envelope correlation coefficient of $\leq$0.002 [38]. Lastly, a dual-band frequency-selective structure based on stepped-impedance loop resonators demonstrates a bandstop response with improved performance under varying incident angles [39]. MIMO antennas showcase their versatility in various applications. Recent studies emphasize two significant designs. The first is a compact dual-polarized Vivaldi antenna, tailored for intelligent Internet of Vehicles (IoV) communications. It demonstrates wide bandwidth, high gain, and isolation, highlighting its efficacy in IoV wireless scenarios [40]. Likewise, a compact quad-element vertically-polarized MIMO antenna, designed for vehicular base stations, excels in bandwidth, port isolation, and mutual coupling reduction, validated through experiments, making it optimal for vehicular communication applications [41]. Further exploration into recent advancements in electromagnetic sensors, as exemplified in [38,39,42], adds valuable depth to our understanding and application domain. These cutting-edge sensors enrich our comprehension of electromagnetic phenomena, providing a nuanced perspective that complements the innovative design and functionality of our advanced sensor for non-invasive breast and brain cancer diagnosis using an antenna array with metamaterial-based AMC. By referencing and analyzing such state-of-the-art electromagnetic sensors, we aim to enhance the readers' grasp of the technological landscape and highlight the significance of our contributions in the context of evolving electromagnetic sensing methodologies. Our research aligns with the design perspective outlined in a recent study on a Metamaterial-Inspired AMC Backed Dual Band Antenna for ISM and RFID Applications. This work emphasizes enhancing gain performance in dual-band frequencies, resonating at 0.915 GHz and 2.45 GHz, crucial for applications in Industrial, Scientific, Medical (ISM), and Radio-frequency Identification (RFID) domains [43].

In this article, we propose and novel antenna and sensor for MWI-based non-invasive early-stage breast and brain cancer diagnosis. The antenna has been developed to advance over devices recently reported in the literature for this purpose. The presented design is based on a microstrip patch antenna coupled with an artificial magnetic conductor (AMC), which allows for considerable gain enhancement. Furthermore, the incorporation of ACM contributes to a creation of an additional and deep resonance within the 2-to-3 GHz band, which is also associated with high gain. An additional effect of the ACM is to create a directive radiation pattern with the main beam oriented in a broadside direction (i.e., perpendicular to the sensor front). All of these features improve the sensor's capacity to detect several types of cancer, including breast and brain tumors. On top of that, ultra-wide bandwidth and a large number of resonances facilitates acquisition of the most precise and complete data during screening. The proposed antenna and sensor have been fabricated and experimentally validated. The measurement results are in good agreement with full-wave simulations. At the operational frequency of about 2.27 GHz, the recorded broadside gain is as high as 11.7 dBi. Extensive simulation studies demonstrate suitability of the proposed design for both breast and brain cancer detection under a variety of scenarios. In addition, our antenna has been compared favorably compared to the state-of-the-art designs reported in the literature, indicating its competitive performance, particularly in terms of application versatility, as well as the size and gain trade-offs.

2. Metamaterial unit cell and AMC design layout

The proposed antenna MWI-based cancer detection has been shown in Fig. 1. Two quarter circles and a half asteroid were chosen as the two geometric designs on the sensor's back surface (cf. Fig. 1(a)) as they facilitate control of the radiation pattern. As shown in Fig. 1(b), the antenna comprises two circular microstrip feeders that are attached to the patch. The major reason for selecting this approach is to maximize the antenna's gain. Two sensors (cf. Fig. 1(c)) are incorporated into the antenna patch and the antenna feeder to magnify the output signal.

The ground's annealed copper structure features a hollow asteroid and a hollow rhombus, crucial for trapping wave produced for specific functions, as shown in Fig. 2(a). The suggested MTM unit cell for a microstrip patch antenna is depicted in Fig. 2(b) and Fig. 2(c). The geometric design of the AMC begins with the unit cell, which serves as the fundamental building block. As depicted in Fig. 2, the unit cell is intricately designed with dimensions that are crucial for achieving the desired electromagnetic properties. Fig. 2(a) offers a rear view of the AMC, providing additional perspective on the structural design and interconnections between unit cells. This comprehensive view allows for a better understanding of the overall architecture and the seamless integration of the AMC with the microstrip patch antenna. The structure includes specific elements indicated by dimensions O, P, and C, each contributing to the overall resonant behavior of the AMC. The design of the unit cell is meticulously optimized to enhance the reflection coefficients and create a resonant frequency that aligns with the operational requirements of the sensor.

Fig. 2(b) illustrates the front view of the AMC array, where multiple unit cells are arranged in a periodic manner to form a 5 × 5 mm^2 grid. This array configuration is essential for the AMC's functionality, as the periodic arrangement of unit cells generates a constructive interference pattern. This pattern significantly improves the frequency selectivity and gain of the antenna, thereby enhancing the precision and quality of the imaging system. The array's design ensures that the AMC can interact effectively with the incident electromagnetic waves, leading to improved performance in detecting anomalies such as tumors.

In Fig. 2(c), the detailed geometric design of an individual unit cell is highlighted. Specific elements, represented by dimensions Q and R, are shown to demonstrate the intricate features that are critical for the unit cell's performance. The precise dimensions and placement of these features are designed to optimize the electromagnetic interaction at the unit cell level. This optimization is crucial for ensuring that the entire AMC array functions effectively, contributing to the enhanced sensitivity and accuracy of the microwave imaging system used for non-invasive breast and brain cancer diagnosis.

The artificial magnetic conductor (AMC) consists of a 5 × 5 array of concentric rhombuses, a vertical line, and two L-shapes on top of the FR4 substrate to enhance the sensor gain. Each annealed copper unit cell is carved on top of the FR4 substrate as shown in Fig. 3. The specific dimensions of the antenna have been shown in Table 1.

3. Simulation results

The sensor's reflection coefficients and realized gain were simulated, revealing that the antenna with AMC resonates at 2.276 GHz, 4.490 GHz, 6.224 GHz, 8.528 GHz, and 9.536 GHz, improving radiation characteristics, as shown in Fig. 4(a). Note that the AMC layer greatly improves impedance matching at 2.276 GHz. This study introduces a novel microstrip patch antenna incorporating an Artificial Magnetic Conductor (AMC) for microwave imaging (MWI) applications in breast and brain cancer diagnosis. Although the design exhibits multiple resonance points, the specific selection of 2.276 GHz offers an optimal balance between penetration depth and resolution, which is crucial for detecting early-stage malignancies. This chosen frequency ensures adequate signal penetration into tissues, allowing the interrogation signal to reach potential tumors, especially in deeper structures such as the breast and brain. Additionally, 2.276 GHz minimizes signal attenuation and dispersion, thereby maintaining high resolution for precise tumor localization and characterization within the acquired image. This balance between penetration depth and resolution is essential for early-stage cancer detection, where abnormalities are often subtle and require accurate identification. Fig. 4(b) displays the sensor's peak realized gain. At the target frequency of 2.276 GHz, the addition of the AMC layer increases the achieved gain by a factor of about 2 dBi. Based on full-wave simulations, the actual gains with and without AMC at the resonant frequency of 2.276 GHz are 8.15 dBi and 10.02 dBi, respectively.

Fig. 5 shows a comparative analysis of the performance of antennas with and without artificial magnetic conductors (AMCs) in the frequency range from 2 to 2.5 GHz. This analysis is important to understand the impact of AMC on antenna parameters such as reflection coefficient and gain, needed to optimize antenna design. In Fig. 5 (a), the simulated reflection coefficient, |S11|, represents the matched impedance, with values close to −40 dB indicating a better fit. The plot compares the antenna with and without AMC, showing improved impedance matching with AMC at 2.276 GHz. Fig. 5(b) shows the simulated broadside gain, shows the directional power concentration of the antenna. AMC affects gain and directivity, improving performance at specific frequencies. The change in gain as a function of frequency highlights the impact of AMC. These simulations are essential for antenna design, showing how AMC improves measures such as impedance and gain matching, thereby contributing to the development of effective application-specific antennas.

The simulated distributions of the magnetic and electric fields corroborate the sensor's high level of dependability. The top and lower halves of the antenna patch at the sensor's front surface exhibit a parallel electrical energy disturbance, as shown in Fig. 6(a). On the right and left sides of the antenna patch, though, magnetic energy may be detected. A further indication that the antenna can capture the magnetic field is the presence of magnetic energy in the antenna's rear portion, as illustrated in Fig. 6(b).

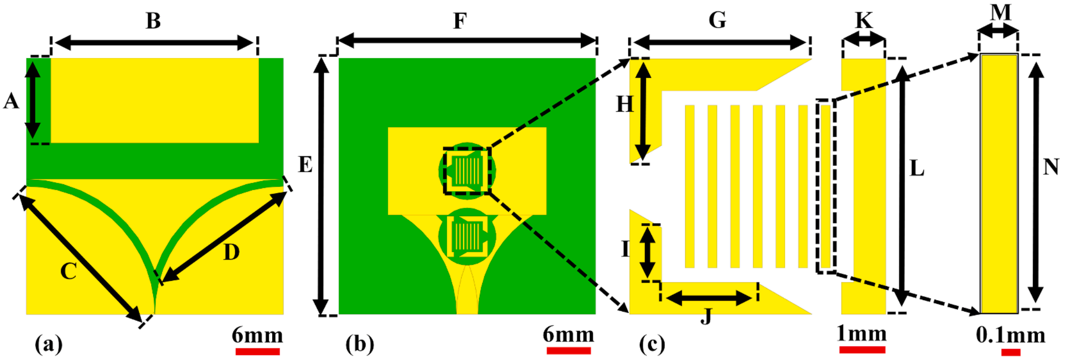

Fig. 1. Geometry of the proposed antenna: (a) back view; (b) front view; (c) antenna resonators.

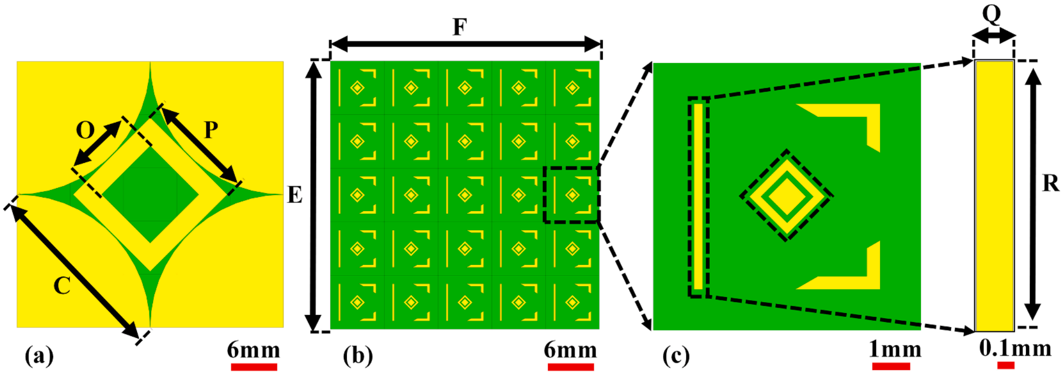

Fig. 2. Geometric design of the AMC: (a) rear view; (b) front view; (c) MTM unit cell geometric design.

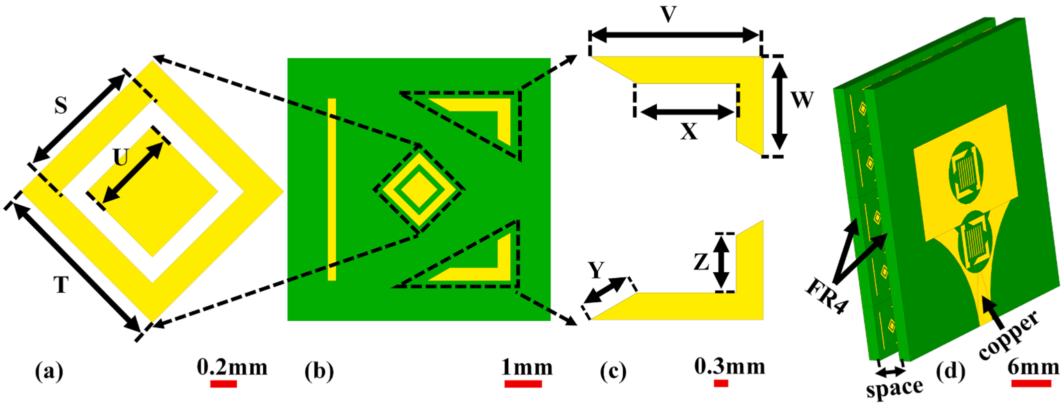

Fig. 3. Geometric design of the MTM unit cells and complete sensor: (a) MTM unit cell rhombus resonators; (b) MTM unit cell geometric design; (c) MTM unit cell L-shapes resonators; (d) sensor after combining the antenna with the AMC.

Table 1
Optimized geometry parameters of the proposed antenna.

Parameter	Value (mm)	Parameter	Value (mm)	Parameter	Value (mm)
A	11.8	J	2.1	S	1
B	28.8	K	0.97	T	1.41
C	25.17	L	5.65	U	0.707
D	21.89	M	0.2	V	2.26
E	35.6	N	3.6	W	1.3
F	35.6	O	9.2	X	1.3
G	4.027	P	14.56	Y	0.707
H	2.32	Q	0.22	Z	0.747
I	1.21	R	5	space	3

Fig. 7(a) depicts the surface current distribution, where high current density areas, indicated by red regions, highlight the critical points of electromagnetic activity. The symmetrical distribution of these currents across the sensor's surface is crucial for maintaining a balanced and efficient radiation pattern. This balance is achieved through the design enhancements provided by the Artificial Magnetic Conductor (AMC), which optimizes the current paths and minimizes losses. This optimization is essential for achieving high gain, as it ensures that the maximum amount of input power is converted into radiated electromagnetic waves, enhancing the overall efficiency and effectiveness of the sensor. Fig. 7(b) shows the power distribution, where the highest power radiation is concentrated and exits from the center of the sensor's front face. The directive nature of this power distribution, indicated by the red regions, is a direct result of the antenna design and the influence

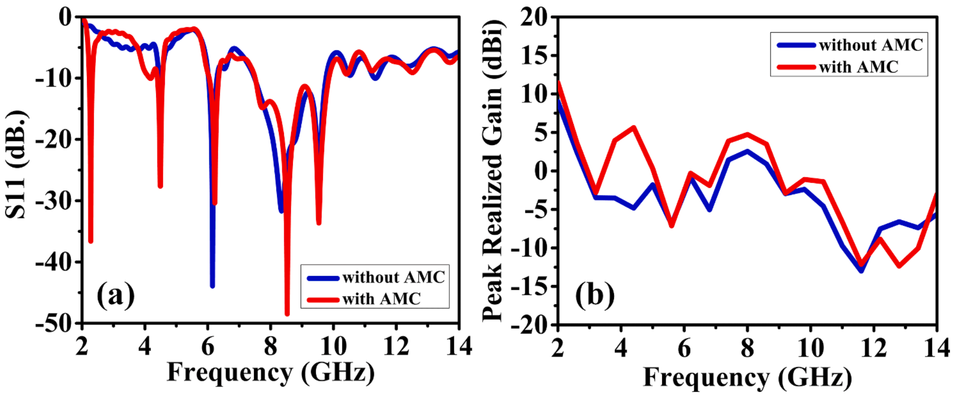

Fig. 4. Antenna with and without AMC: (a) simulated reflection coefficient $|S_{11}|$; (b) simulated broadside gain.

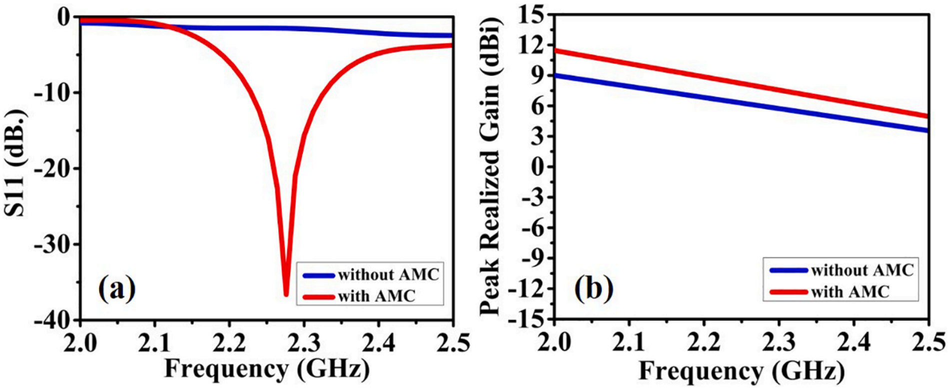

Fig. 5. Antenna with and without AMC 2-to-2.5 GHz range.: (a) simulated reflection coefficient $|S_{11}|$; (b) simulated broadside gain.

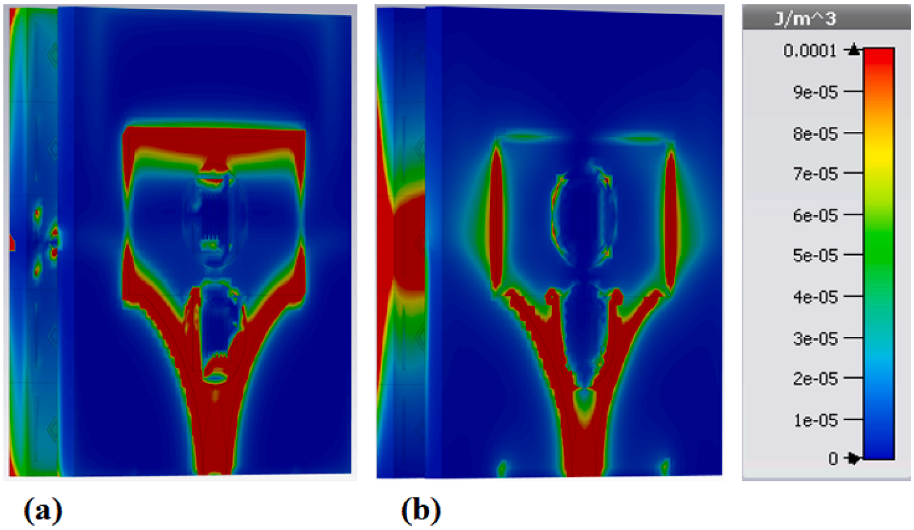

Fig. 6. Energy density at 2.276 GHz: (a) E-field; (b) H-field.

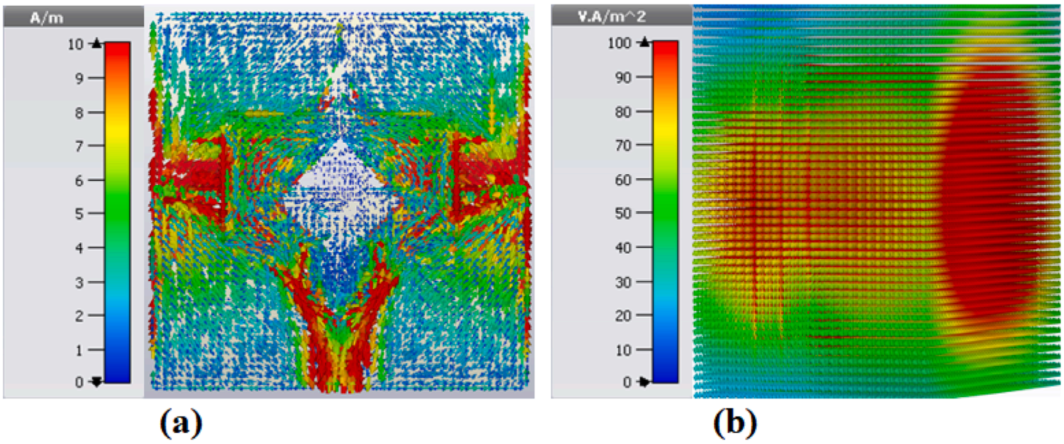

Fig. 7. The sensor operating at 2.276 GHz: (a) surface current distribution; (b) power distribution.

of the AMC. The AMC improves the antenna's impedance matching and creates an additional resonance at 2.276 GHz, which enhances the antenna's selectivity and directivity. This directed radiation pattern ensures that the radiated energy is focused towards the target area, which is vital for high-resolution imaging required in medical diagnostics. The ability to focus energy precisely increases the sensor's effectiveness in detecting small anomalies, such as early-stage cancer cells, by providing clearer and more detailed images.

Radiation pattern is another property that is essential from the perspective of medical applications. It clarifies, in particular, how trustworthy the sensor is for experts in breast and brain cancer early detection. Fig. 8(a) shows that the radiation pattern of the antenna without an AMC will point in the opposite direction at an angle of 180°. The radiation direction of the pattern will be at an angle of 0° and

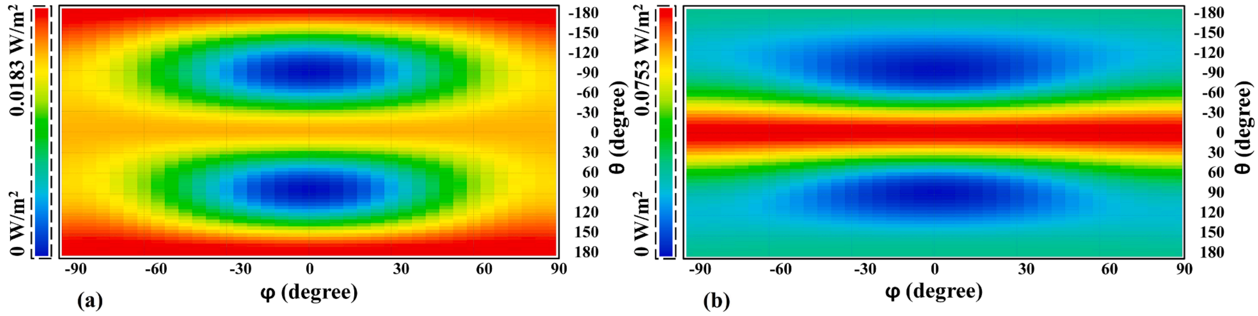

Fig. 8. 2D simulation of the proposed antenna's radiation pattern at 2.276 GHz with $\phi = 90$: (a) without AMC; and (b) with AMC.

radiated from the center of the sensor when the AMC is applied to the suggested antenna, as shown in Fig. 8(b). The latter corroborates suitability of the sensor for breast and brain cancer detection. Fig. 8 presents a 2D simulation of the proposed antenna's radiation pattern at 2.276 GHz with $\varphi = 90^\circ$. In Fig. 8(a), without the Artificial Magnetic Conductor (AMC), the antenna demonstrates a broad and diffuse electromagnetic field distribution characterized by low gain and wide beamwidth. The lower peak power density (0.0183 W/m^2) and wider angular spread of the radiation pattern indicate reduced efficiency in focusing electromagnetic energy, which can negatively impact imaging applications by providing less directed emission. Conversely, Fig. 8(b) illustrates the radiation pattern with the inclusion of AMC, showing significant enhancements in radiation characteristics. The presence of the AMC results in a higher peak power density (0.0753 W/m^2) and a narrower beamwidth. This improved pattern, with more concentrated and directed primary lobes, enhances impedance matching, reduces reflection losses, and optimizes the antenna's frequency response at 2.276 GHz. These improvements in directivity and gain are crucial for high-resolution imaging, enabling the sensor to more accurately and effectively detect small anomalies such as early-stage cancer cells, thereby improving the resolution and clarity of images in medical applications.

The incorporation of an Artificial Magnetic Conductor (AMC) significantly enhances the proposed antenna's performance for microwave imaging applications, particularly beneficial for early-stage breast and brain cancer detection. The AMC introduces an additional resonance peak at 2.276 GHz, improving frequency selectivity for focusing on the signal of interest. It also influences current distribution to achieve higher gain and a more directive radiation pattern, concentrating the emitted energy towards the target tissue. Furthermore, the AMC optimizes impedance matching for efficient power transfer and reduces interference through its directive radiation profile. These combined effects, demonstrably validated by our experimental results and simulations (increased gain of 11.7 dBi), highlight the crucial role of AMC in enhancing the proposed sensor's functionality for early-stage cancer detection.

The inclusion of an artificial magnetic conductor (AMC) significantly impacts the antenna's performance, enhancing both network and radiation parameters for microwave imaging applications. AMC introduces additional frequency selectivity, observed in our design by the new resonance peak. This sharper response allows for more efficient energy transfer between the antenna and biological tissues at the desired frequency. Furthermore, the AMC's influence on surface currents can improve impedance matching and contribute to a more directive radiation pattern. This directivity, with potentially higher gain levels achieved through AMC, is crucial for accurate microwave imaging. Overall, AMC integration enhances the antenna's suitability for non-invasive cancer diagnosis by improving its ability to target tissues and achieve high-quality imaging.

Fig. 9 presents the real and imaginary parts of permeability (μ) and permittivity (ϵ) for the proposed AMC, which are essential for understanding its electromagnetic behavior across different frequencies. The calculation of these properties is based on several key equations related to metamaterials (MTMs).

The relative permittivity (ϵr) can be calculated using Eq. (1) [26,44]:

$$\varepsilon_r = \frac{1}{\mu_r}\left[\left[\frac{\omega_c}{\omega}\right]^2 - \left[\frac{1}{\omega d\sqrt{\mu_0\varepsilon_0}}\ln(\xi)\right]^2\right] \qquad (1)$$

where μr is the relative permeability, ω is the angular frequency, ωc is the angular cutoff frequency of the incident wave, d is the maximum length of the metamaterial unit cell, and ξ is a parameter defined in Eq. (2):

$$\xi = EXP\left(j\omega d\sqrt{\mu_0\varepsilon_0\left(n^2 - \left(\frac{\omega_c}{\omega}\right)^2\right)}\right) \qquad (2)$$

Alternatively, ξ can also be expressed as shown in Eq. (3):

$$\xi = \frac{1-(S_{11}+S_{21})\Gamma}{S_{11}+S_{21}-\Gamma} \qquad (3)$$

Here, $S11$ and $S21$ are the reflection and transmission coefficients,

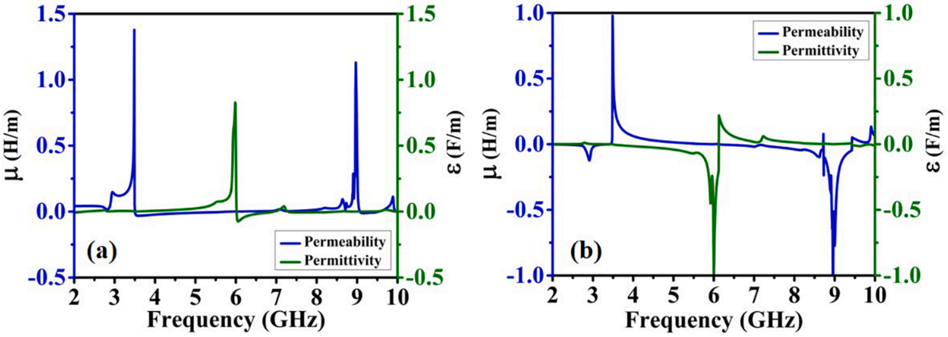

Fig. 9. (a) Real parts of Permeability (μ') and Permittivity (ϵ'), (b) Imaginary parts of Permeability (μ'') and Permittivity (ϵ'') of the proposed absorber.

respectively, and Γ is defined in Eq. (4):

$$\Gamma = \frac{S_{11}^2 - S_{21}^2 + 1}{2S_{11}} \pm \left[\left(\frac{S_{11}^2 - S_{21}^2 + 1}{2S_{11}} \right)^2 - 1 \right]^{\frac{1}{2}} \tag{4}$$

The relative permeability (μr) is calculated using Eq. (5) [26,44]:

$$\mu_r = \frac{1+\Gamma}{1-\Gamma} \left[n^2 - \left(\frac{\omega_c}{\omega} \right)^2 \right]^{\frac{1}{2}} \left[1 - \left(\frac{\omega_c}{\omega} \right)^2 \right]^{\frac{-1}{2}} \tag{5}$$

where n is the refractive index.

These relationships provide a detailed understanding of the electromagnetic properties of the metamaterial used in the AMC. The resonance points observed in Fig. 9 correspond to the specific frequencies at which the permeability and permittivity values exhibit significant peaks. These peaks indicate the effective tuning of the metamaterial's response to electromagnetic waves, which is crucial for applications like microwave imaging in non-invasive cancer detection. By using these equations, the behavior of the metamaterial can be accurately modeled and understood.

Fig. 9 presents the frequency-dependent behavior of the real and imaginary parts of the permeability (μ) and permittivity ($\in$) for the proposed AMC. The plots in Fig. 9(a) illustrate the real parts of permeability (μ') and permittivity ($\in'$), while Fig. 9(b) shows the corresponding imaginary parts (μ'' and $\in''$). These parameters are critical for understanding the electromagnetic properties and performance of the absorber in conjunction with the antenna.

In Fig. 9(a), the real part of permeability (μ') demonstrates multiple resonance peaks at frequencies 2.276 GHz, 4.490 GHz, 6.224 GHz, 8.528 GHz, and 9.536 GHz, indicating the material's magnetic resonance at these specific frequencies. This behavior suggests that the material supports the formation of a magnetic field, which is crucial for its application in electromagnetic absorption. Similarly, the real part of permittivity ($\in'$) remains relatively constant with minor variations, showing slight peaks corresponding to the observed magnetic resonances. This coupling between electric and magnetic properties highlights the material's ability to store electrical energy efficiently.

Fig. 9(b) shows the imaginary parts of permeability (μ'') and permittivity ($\in''$), which represent the magnetic and dielectric losses, respectively. The imaginary permeability (μ'') exhibits peaks at the same resonance frequencies, indicating magnetic energy absorption and loss. The negative values observed in μ'' suggest efficient energy absorption at these frequencies, typical of metamaterials designed for such purposes. The imaginary permittivity ($\in''$) also displays peaks at the same resonance points, indicating dielectric losses and the material's ability to dissipate electrical energy. These resonance and loss characteristics are crucial for optimizing the absorber's performance, particularly in enhancing the antenna's functionality for non-invasive medical imaging applications. The integration of AMC enhances these resonances, particularly at the first resonance frequency of 2.276 GHz, underscoring its role in tailoring the absorber's electromagnetic properties for precise frequency responses required in applications like early-stage cancer detection using microwave imaging.

Fig. 10 illustrates the simulated responses of the refractive index and impedance parameters for the proposed metamaterial absorber, providing insight into the material's electromagnetic properties across a frequency range of 2 GHz to 10 GHz.

Fig. 10(a) depicts the real and imaginary parts of the refractive index, where the real part (blue line) fluctuates between approximately 0 and 0.035, while the imaginary part (red line) oscillates around −0.01 to 0.02. These characteristics were derived using Eq. (4), where n is the refractive index calculated from the relative permeability (μr) and relative permittivity (εr) parameters, demonstrating the metamaterial's influence on the phase velocity and absorption of electromagnetic waves.

Fig. 10(b) shows the real and imaginary parts of the impedance (z). The real part (blue line) exhibits pronounced peaks at specific frequencies, notably at 2.276 GHz, 4.490 GHz, 6.224 GHz, 8.528 GHz, and 9.536 GHz, aligning with the resonance points achieved after the addition of the AMC to the antenna. These peaks indicate optimal impedance matching with the free-space characteristic impedance, facilitating maximum power transfer. The imaginary part of the impedance (red line) presents sharp transitions at these resonance frequencies, indicating variations in reactive energy storage.

The analysis of both figures highlights the relationship between the electromagnetic parameters of permeability and permittivity (as shown in the earlier figure) and the derived parameters of refractive index and impedance. The resonance frequencies observed in the permeability and permittivity plots correspond to the peaks in the real parts of the refractive index and impedance, validating the effectiveness of the AMC in tuning the antenna's performance. The five resonance points achieved, particularly the added resonance at 2.276 GHz, underscore the AMC's role in enhancing the antenna's functionality by optimizing its electromagnetic characteristics across the specified frequency range.

Fig. 11 illustrates the electromagnetic properties and group delay variations of the antenna combined. In Fig. 11(a), the reflectance (green curve) shows high peaks at specific wavelengths, indicating significant reflection of incident electromagnetic waves by the AMC at these points. The transmittance (red curve) remains low across the wavelength range, demonstrating that the AMC effectively blocks most incident waves from passing through. Absorbance (brown curve) exhibits peaks corresponding to the absorption of electromagnetic energy at certain wavelengths. These characteristics collectively suggest that the AMC is designed to enhance the antenna's performance by selectively reflecting and absorbing electromagnetic waves, thereby optimizing resonance at specific frequencies.

Fig. 11(b) presents the group delay variations for two configurations: face to face (FtF) and side by side (SbS). The group delay, defined by

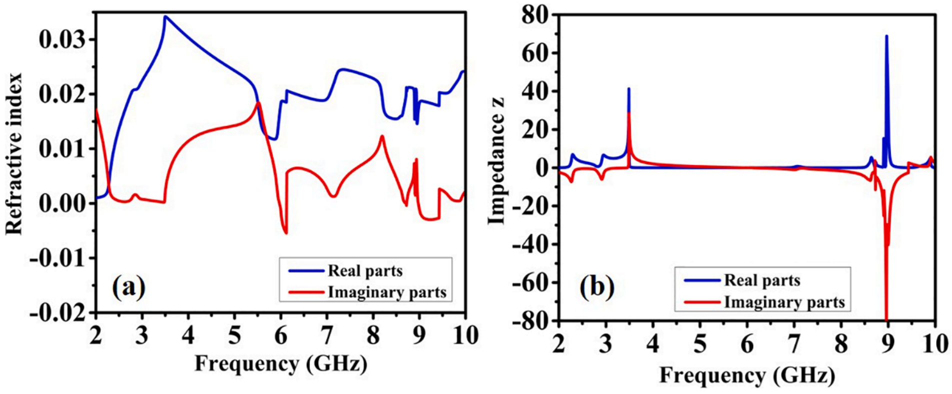

Fig. 10. The simulated responses of parameters, Real parts and Imaginary parts: (a) Refractive index, (b) Impedance z.

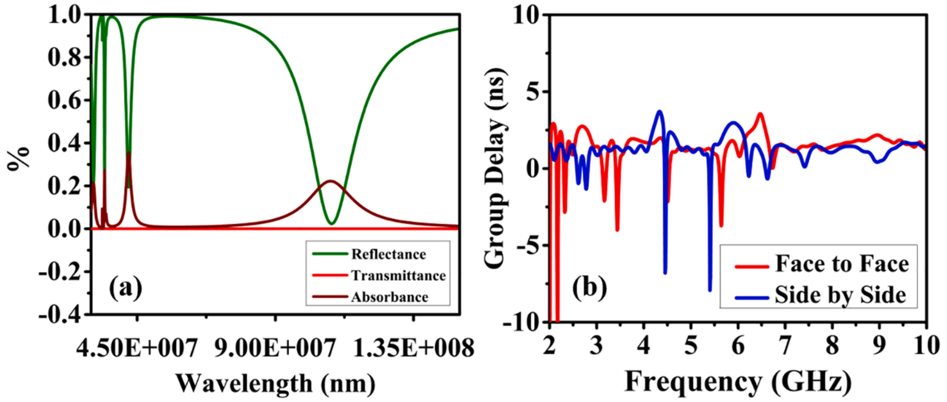

Fig. 11. (a) AMC characteristics transmittance, absorbance, and reflectance, (b) The group delay variation for FtF and SbS.

$$\tau = -\frac{d\theta(\omega)}{d(\omega)} \tag{6}$$

where $\theta(\omega)$ is the signal phase and ω is the angular frequency, reveals the time delay experienced by the signal's envelope as it propagates through the system. The FtF configuration (red curve) shows significant fluctuations across the frequency spectrum due to direct interactions and reflections between the antennas. Conversely, the SbS configuration (blue curve) exhibits different group delay patterns, reflecting the altered propagation dynamics in this arrangement. Notably, the resonance points at 2.276 GHz, 4.490 GHz, 6.224 GHz, 8.528 GHz, and 9.536 GHz correspond to distinctive features in the group delay plot, underscoring the AMC's impact on phase behavior and signal propagation.

Fig. 12 presents a time-domain analysis of the transmitted and received pulses for two configurations: side-by-side (SbS) and face-to-face (FtF). This analysis is critical for evaluating the performance of the Microwave Imaging (MWI) system, as it provides insights into the signal integrity and propagation characteristics. In Fig. 12(a), the SbS configuration shows the input pulse (blue) and the received pulse (red) with both sensors placed side by side at a distance of 200 mm. The received pulse closely follows the input pulse, indicating minimal distortion and reliable signal transmission. This configuration demonstrates the system's ability to maintain the signal's integrity even when the sensors are laterally positioned. Fig. 12(b) illustrates the FtF configuration, where the sensors are positioned face to face at the same distance. The input pulse (blue) and the received pulse (red) in this configuration also show a high degree of correlation, indicating that the system effectively transmits and receives the pulse with minimal distortion. The FtF configuration benefits from the direct alignment of the sensors with the radiation pattern, ensuring that the signal is captured with high fidelity. This alignment is particularly crucial for obtaining reliable and high-quality images in MWI applications, as it maximizes the signal-to-noise ratio and reduces potential interference from surrounding environments.

The choice of the FtF configuration is driven by the need for optimal directional radiation and reception, which is essential for high-resolution imaging. While both configurations show close results, the FtF setup provides a more controlled and directed signal path, enhancing the reliability and quality of the captured images. This alignment ensures that the signal propagates directly between the sensors without significant multipath effects, leading to more accurate and precise imaging outcomes. The time-domain analysis in Fig. 12 thus underscores the importance of sensor orientation and alignment in achieving superior performance in MWI systems.

4. Experimental validation

This section discusses experimental validation of the antenna structure and sensor introduced in Section 3. In particular, we elaborate on the fabrication process, experimental setup, as well as results concerning the major antenna characteristics, including impedance matching, gain, and radiation patterns.

4.1. Antenna prototype

The proposed antenna has been implemented on the 1.52-mm-thick FR4 substrate according to the geometrical dimensions reported in Table 1. The device has been manufactured using the LPKF protolaser machine. The photographs of the antenna and the AMC prototypes have been shown in Fig. 13 and Fig. 14, respectively. Fig. 15 shows a perspective view of the complete sensor.

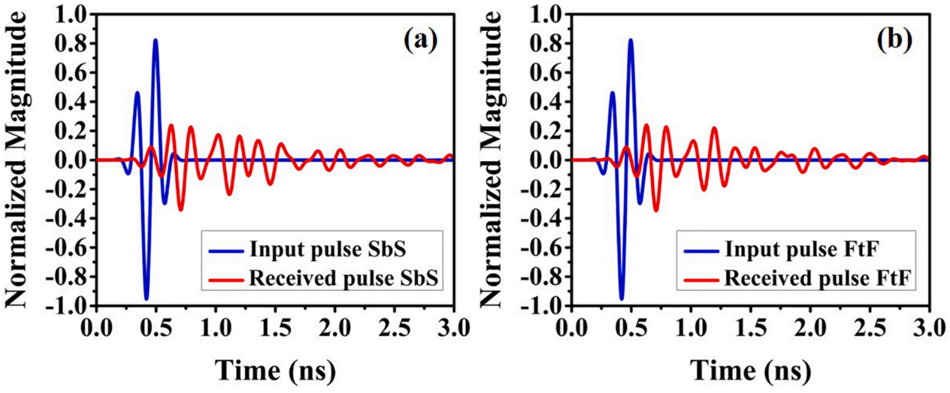

Fig. 12. Normalized Transmitted and received pulse in: (a) Side by Side, (b) Face to Face.

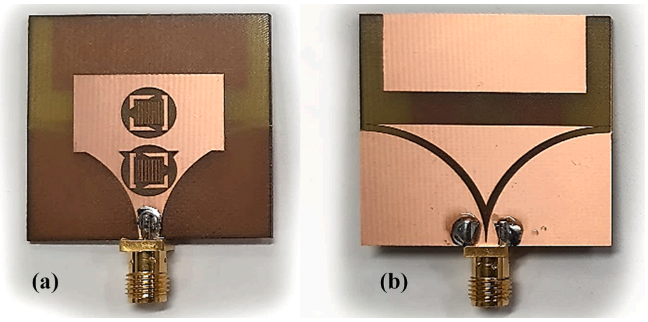

Fig. 13. Photographs of the antenna prototype: (a) front view, (b) back view.

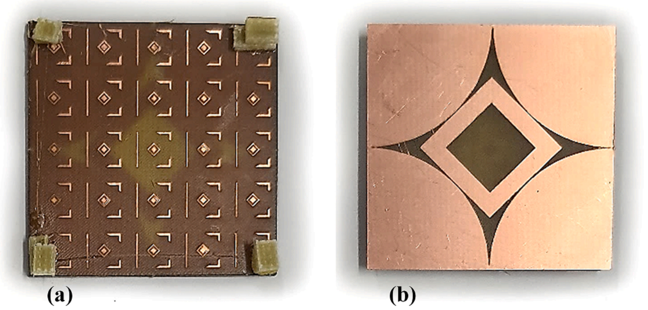

Fig. 14. Photographs of the AMC prototype: (a) front view, (b) back view.

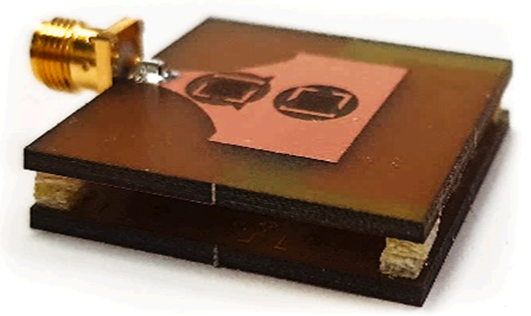

Fig. 15. Photograph of the assembled sensor prototype: perspective view.

4.2. *Experimental setup*

The electrical and field performance parameters of the antenna, including its reflection response, gain, and radiation patterns, have been measured in a fully-calibrated anechoic chamber of Reykjavik University, Iceland. The measurements have been carried out using 0–40 GHz Anritsu MS4644B vector network analyzer (VNA), and Geozondas GZ0226DRH 2–26 GHz horn antenna. A photograph of the measurement setup has been shown in Fig. 16.

4.3. *Impedance matching and realized gain*

The reflection and realized gain characteristics of the antenna with and without the AMC are compared in Fig. 17 and Fig. 18, respectively. Fig. 17(a) shows the measured and simulated reflection coefficient without AMC. The impedance matching without AMC assistance exhibit a sharp decline in efficiency, suggesting possible difficulties in precisely identifying early-stage cancer. The results show a wide, multi-resonant bandwidth, but there is no resonance between 2 and 3 GHz. The slight differences between simulation and measurement are observed, which can be attributed to manufacturing and assembly imperfections. These variations emphasize the demand for more advanced antenna technology in cancer diagnosis. The reflection responses of AMC-supported antenna are presented in Fig. 17(b). Attaching the AMC results in an additional resonance created at the frequency around 2.27 GHz. The performance of antennas is thereby improved from the perspective of enabling more precise and consistent identification of cancer cells in their early stages. The adoption of AMC technology can also lessen interference from neighboring tissues, increasing the diagnostic accuracy even more. In particular, the presence of a high-gain resonance between 2 and 3 GHz is caused by the zero return of electromagnetic waves, cf. Fig. 18. Realization of artificial magnetic field provided by the AMC unit, prevents returning of electromagnetic waves from the antenna in the back (source) direction, which results in the mentioned resonance associated with high gain. As indicated in Fig. 18, there are only minor differences between the simulated and measured results. At the same time, the achieved ultra-wideband characteristic of the antenna plays a significant role in the imaging quality with microwave techniques for early-stage cancer detection.

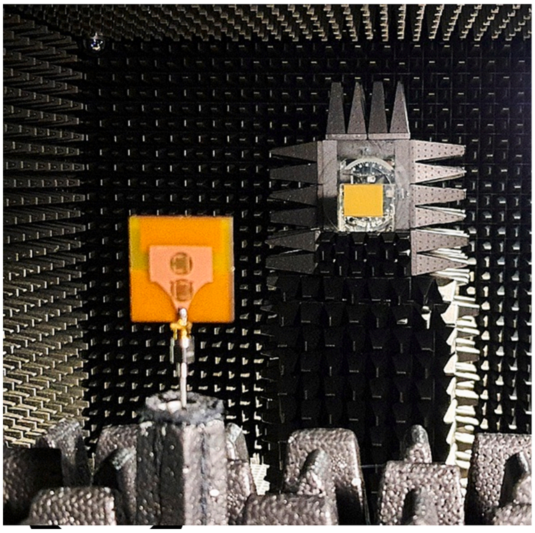

Fig. 16. Measurement setup of the proposed antenna in an anechoic chamber.

Metallic constructions are susceptible to surface waves because of their smooth, flat sides, which permit electromagnetic waves to pass between the metal and its surroundings [45]. When a surface wave comes into contact with bending, deformation, or irregular surface patterns, it radiates vertically in the microwave stream. The proposed antenna has gaps or fractures in the ground plane that cause interruptions. As a result, the surface wave that is exposed to this discontinuity is transmitted vertically with no phase reflection to the AMC structure that is situated on the antenna’s trailing side. Additionally, AMC reflects recently developed electromagnetic waves. Consequently, the AMC’s constructive integration of the electromagnetic waves into the radiated wave increases the total gain of the antenna [46].

At the frequency of 2.276 GHz, the proposed AMC structure displays zero reflection phase, leading to a significant gain increase. The identification of cancer cells in their early stages can therefore be made more precise. Furthermore, the antenna’s small size makes it appropriate for non-invasive and portable diagnostic instruments. Impedance matching between the AMC and antenna is necessary to achieve null reflective phase properties. For that, a gap of 3 mm between the AMC and the antenna was selected, as indicated in Table 1. Cross-coupling causes poor impedance matching and reflection with zero-phase quality when the distance is less than or greater than 3 mm. Fig. 18(a) depicts the broadside gain attained by the antenna with AMC. The gain is particularly high within the frequency range between 2 and 3 GHz, as shown in Fig. 18(b). In particular, the broadside gain at the resonant frequency of

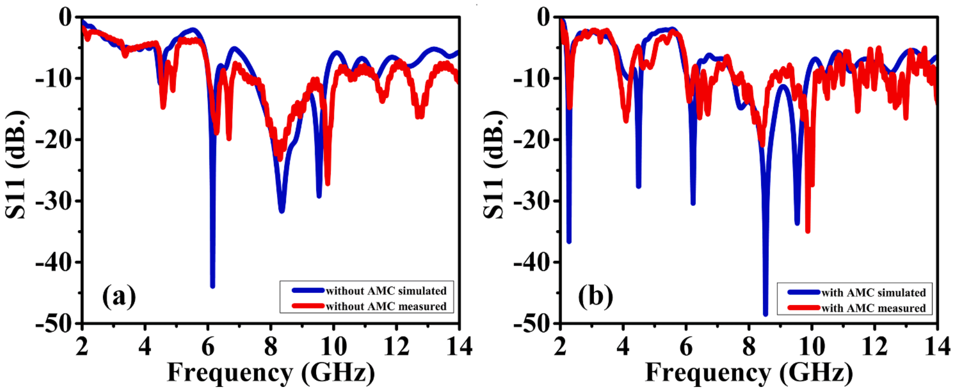

Fig. 17. Simulated and measured reflection characteristics of the proposed antenna: (a) without AMC, (b) with AMC.

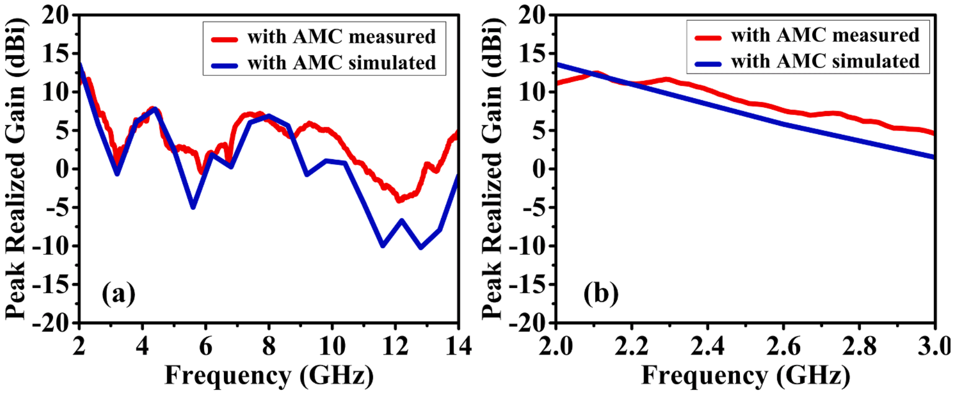

Fig. 18. Simulated and measured broadside realized gain responses: (a) broadband responses, (b) 2-to-3 GHz range.

2.276 GHz is 11.7 dBi.

4.4. Radiation patterns

Fig. 19(a) and Fig. 19(b) show the EM-simulated and measured E- and H-plane radiation patterns of the antenna, respectively. These patterns correspond to the azimuth angles $\varphi = 90$ and 0 degrees, respectively. These results demonstrate that the patterns are directional. Furthermore, the agreement between simulations and measurements is satisfactory. The measurements are expressed in the tables of spherical coordinates theta θ and phi φ, respectively. The spherical coordinates are related to the Cartesian axes as follows: θ from 0 to 360 and phi $\varphi = 0$ corresponds to the *xz*-plane (or E-plane), $\varphi = 90$ corresponds to the *yz*-plane (or H-plane), whereas $\theta = 90$ (with variable phi) corresponds to the *xy*-plane [9,17]. The antenna's E- and H-plane radiation patterns are crucial because they give information about the antenna's directivity and coverage in various planes. In particular, this allows for a better understanding how the antenna transmits energy and interacts with nearby objects or tissues. In the context of microwave imaging, it also evaluates the antenna's capacity to identify and localize malignant cells within the body, thereby facilitating MWI system design.

It should be emphasized that the employment of metamaterials as an artificial magnetic conductor also has interesting consequences for antenna properties. In particular, the antenna becomes unidirectional when the AMC destination configuration is applied. As a consequence, the antenna's performance improved. The primary lobes' orientation is

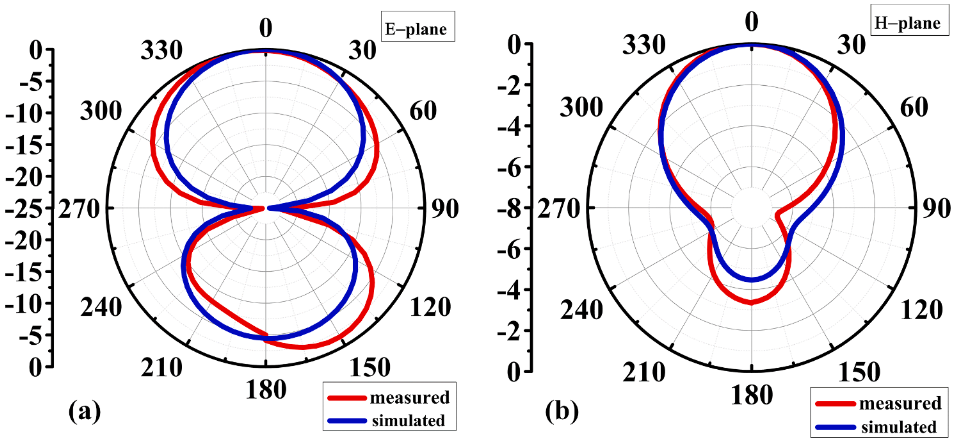

Fig. 19. Measured and simulated 2D normalized radiation patterns of the proposed sensor with AMC at 2.276 GHz: (a) φ = 90, (b) φ = 0.

unaffected by the broadside beam; hence, E-plane and H-plane beams are used. The effectiveness of the sensor for early breast and brain cancer detection will be highlighted in Section 5. As discussed earlier, utilization of AMC greatly improves antenna reflection, leading to reducing the amount of energy losses [9,47].

5. Breast cancer diagnosis

The antenna is appropriate for tumor detection and microwave imaging of breasts due to its performance in the frequency and temporal domains. For the sake of demonstration, we employ a breast model which includes five layers, as shown in Fig. 20(a), and a 95 % early detection pass rate. Fig. 20(b) displays four copies of the proposed antenna for breast tumor detection. Multiple tumors show that cancer cells have grown and spread, which is not the intended outcome. The characteristics of these several levels are shown in Table 2.

The study examines distinguishing normal breasts from newly cancerous ones using scattered signals in early breast cancer stages, with 99 % [5] and 97 % [48] survival rates. As demonstrated in Fig. 21(a), there is a significant difference between the signals of a clean breast and a newly malignant breast in the frequency range from 3.5 GHz to 3.7 GHz. This difference in an oscillator is 0.036 GHz, or 36 MHz. The signal of a normal breast and that of a newly malignant breast differ significantly in the frequency range of 6.3 GHz to 6.39 GHz, with a difference of 0.012 GHz, or 12 MHz, between them, as shown in Fig. 21(b). The observed frequency shift in the reflection coefficient of the breast phantom with a tumor present is a critical indicator of the tumor's presence and its impact on the electromagnetic properties of the tissue. When a tumor is introduced into the breast phantom, it alters the electrical properties of the tissue, specifically the permittivity and conductivity. Tumorous tissues typically exhibit higher permittivity and conductivity due to their increased water content and cellular density compared to normal tissues. This variation in electrical properties leads to a change in the effective dielectric constant of the phantom, resulting in a shift in the resonant frequency of the antenna-phantom system.

The shift in the resonant frequency can be understood by considering the electromagnetic wave propagation through the tissue. The higher permittivity of the tumor increases the effective permittivity of the medium, which in turn affects the phase velocity of the wave. This change in phase velocity leads to a shift in the resonant frequency, which is observed as a deviation in the reflection coefficient. The presence of the tumor modifies the boundary conditions and the overall impedance of the system, leading to a distinct frequency shift that can be detected by the antenna. This shift is a direct consequence of the interaction between the electromagnetic waves and the altered dielectric properties of the tumorous tissue.

The provided reflection coefficient plots (Fig. 21) clearly illustrate this phenomenon. The comparative analysis of the reflection coefficients for both scenarios (phantom with and without tumor) shows a noticeable frequency shift. For instance, the reflection coefficients $|S21|$ and $|S41|$ in the presence of a tumor shift to a lower frequency compared to the normal tissue. This shift is a result of the increased permittivity of the tumor, which reduces the resonant frequency of the antenna-phantom system. Similarly, the $|S31|$ reflection coefficient plot demonstrates a similar frequency shift, further corroborating the impact of the tumor on the antenna's response.

In conclusion, the frequency shift observed in the reflection coefficient due to the presence of a tumor is a vital indicator of the changes in the electromagnetic properties of the tissue. This shift enhances the sensitivity and selectivity of the proposed antenna system, enabling accurate detection and localization of tumors in a non-invasive manner. The detailed analysis of the reflection coefficient behavior and the corresponding frequency shift underscores the practical application of our sensor for early-stage cancer diagnosis, offering a reliable and precise method for detecting abnormalities in breast tissue.

The captured data from the proposed antenna array necessitates meticulous signal processing to generate high-quality images for cancer diagnosis. This processing chain plays a critical role in translating the raw data into interpretable information about the internal tissue composition.

The initial stage involves pre-processing the raw data from the antenna array. This step aims to remove unwanted noise and artifacts introduced during the measurement process. Common techniques include filtering to eliminate background noise and calibration procedures to account for systematic errors in the measurement system. After pre-processing, advanced imaging algorithms are employed to reconstruct the spatial distribution of electrical properties (permittivity and conductivity) within the tissue based on the scattered electromagnetic waves received by the antenna array. These algorithms leverage the principles of inverse scattering, where the scattered field information is used to infer the properties of the scattering object (i.e., the human body with potential tumors). Popular approaches include iterative techniques that progressively refine an initial guess of the tissue properties or compressed sensing methods that exploit sparsity assumptions in the permittivity and conductivity distributions.

Following the reconstruction process, post-processing techniques are applied to enhance the visualization of potential anomalies within the reconstructed image. Common methods include image filtering to suppress background clutter and thresholding to differentiate between healthy and cancerous tissues based on their distinct electrical properties. By effectively processing the captured data, these techniques enable the visualization of potential tumors within the reconstructed image, aiding medical professionals in early cancer diagnosis and treatment planning.

Microwave imaging explores the electrical characteristics of healthy cells and tissues to contrast newly infected cancer cells or tumors with those of healthy cells and tissues. The sensor was used in three cases: a pure breast phantom, non-invasive (early-stage) cancer with a tumor of a 3 mm radius, and invasive cancer with multiple tumors. The first tumor was located within the fibro-glandular tissue, while the second

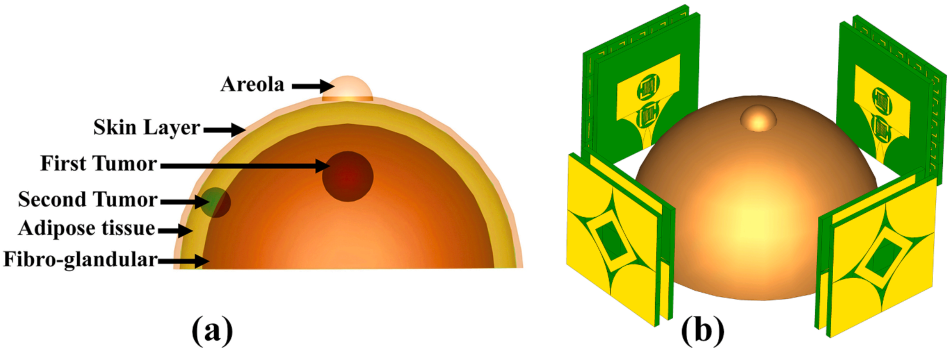

Fig. 20. Application of the proposed antenna for breast cancer detection: (a) cancerous breast phantom; (b) MWI system simulation setup.

Table 2
Dielectric properties of the human breast tissues with tumor and malignant cells.

Tissue Type	Effective Dielectric Permittivity (ε_{eff}) (F/m) [10,11,16]	Electric or Effective Conductivity (σ_{eff}) (S/m) [10,11,16]	Density (kg/m^3) [10,11]	Thermal Conductivity (W/K·m) [49]	Specific Heat Capacity (kJ/K.kg) [49]	Diffusivity (m^2/s)
Areola	36.7	2.34	1109	0.52	3.92	1.19615×10^{-7}
Skin	36.7	2.34	1109	0.52	3.92	1.19615×10^{-7}
Adipose tissue	4.84	0.262	911	0.23	1.9	1.32879×10^{-7}
Fibro-glandular	20.1	0.5	1035	0.51	3.9	1.26347×10^{-7}
Tumor	67	4	1085	0.55	3.75	1.35177×10^{-7}
Malignant cell	15.12	2.346	1085	0.55	3.75	1.35177×10^{-7}

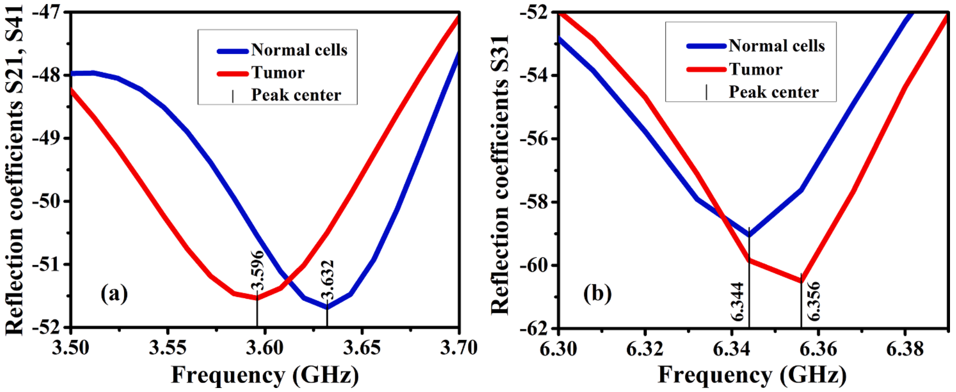

Fig. 21. Reflection coefficient in the breast phantom with a tumor present: (a) $|S_{21}|$ and $|S_{41}|$, (b) $|S_{31}|$.

tumor was partially in the fibro-glandular and adipose tissue. The distance between the two tumors was 22 mm, with the second tumor having a smaller radius of 1.5 mm. Tumors increase electric field concentration, which aids in the diagnosis and localization of tumors in breast tissue, as seen in Fig. 22. By analyzing backscattering signals, our suggested system accurately detects tumors, making it a good contender for microwave breast imaging.

Fig. 23 shows that the magnetic field is more localized around the phantom when no tumor is present, distributed at the center when a tumor is present, and distributed around the tumor's location.

The size of the tumor in six cases of noninvasive (early-stage) breast cancer was thoroughly examined. According to Fig. 24(b), the first case had a tumor with a radius of 0.5 mm. Furthermore, Fig. 24(c) illustrates the presence of a tumor in the second case with a radius of 1 mm. The third case exhibited a tumor with a 1.5 mm radius, as shown in Fig. 25 (b). Additionally, Fig. 25(c) shows that a tumor with a 2 mm radius was seen in the fourth case. The tumors in the fifth case, as shown in Fig. 26 (b), had a 2.5 mm radius. Additionally, Fig. 26(c) shows that the sixth case had a tumor with a 3 mm radius.

6. Brain cancer diagnosis

Microwave imaging (MWI) leverages the distinct electrical properties of healthy and cancerous tissues, specifically the permittivity and conductivity. While these properties vary between breast and brain tissues, cancerous lesions generally exhibit a noticeable contrast compared to surrounding healthy tissue in both organs. Our sensor system is strategically designed to operate at a frequency where this contrast is optimally utilized, ensuring effective differentiation between normal and abnormal tissues in breast and brain cancer diagnosis.

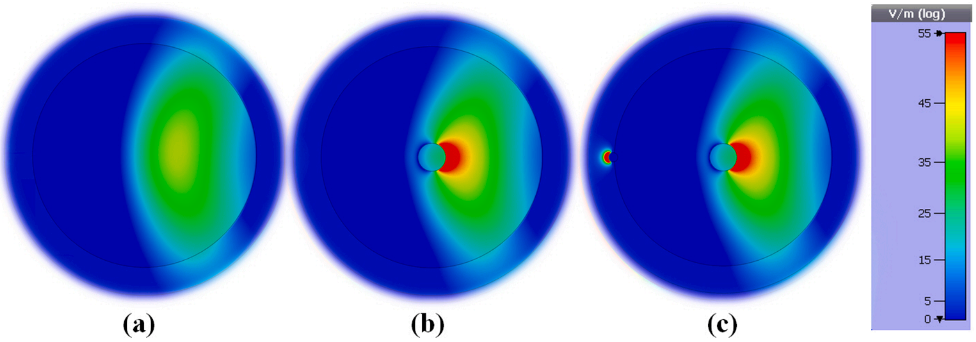

Fig. 22. E-field microwave imaging technique results at 2.276 GHz: (a) normal; (b) non-invasive breast cancer with one tumor; and (c) invasive breast cancer with two tumors.

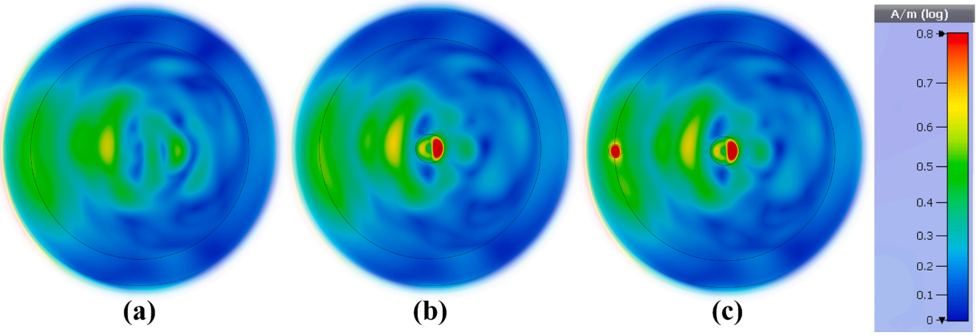

Fig. 23. H-field microwave imaging technique results at 2.276 GHz: (a) normal; (b) non-invasive breast cancer with one tumor; and (c) invasive breast cancer with two tumors.

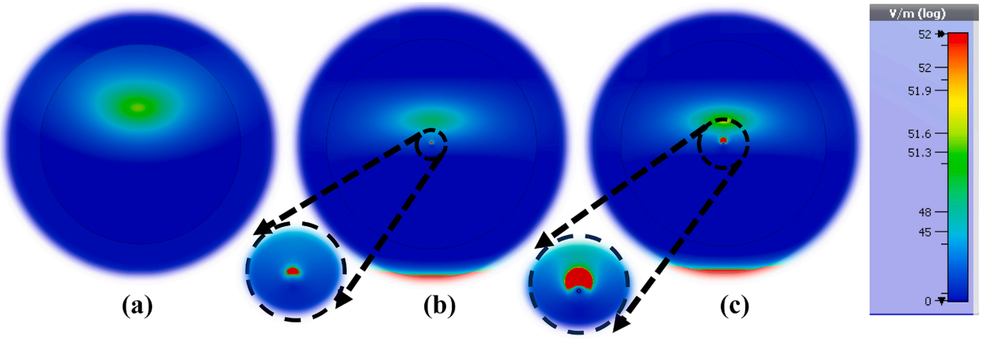

Fig. 24. MWI at 2.276 GHz, an E-field microwave imaging approach was used to evaluate tumor volume change: (a) normal; (b) first case; (c) second case.

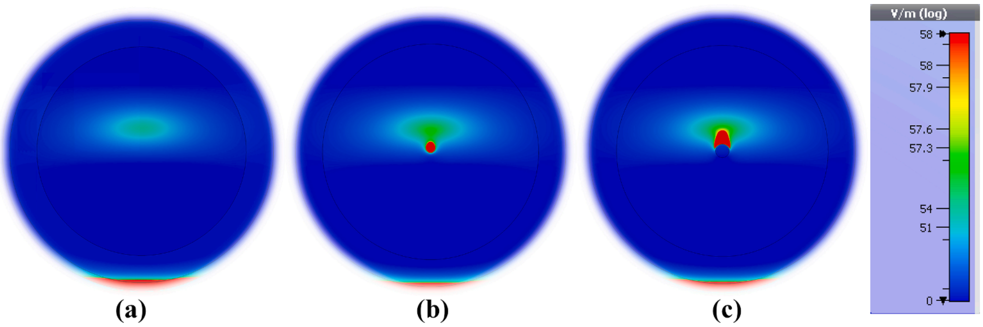

Fig. 25. MWI at 2.276 GHz, an E-field microwave imaging approach was used to evaluate tumor volume change: (a) normal; (b) third case; (c) fourth case.

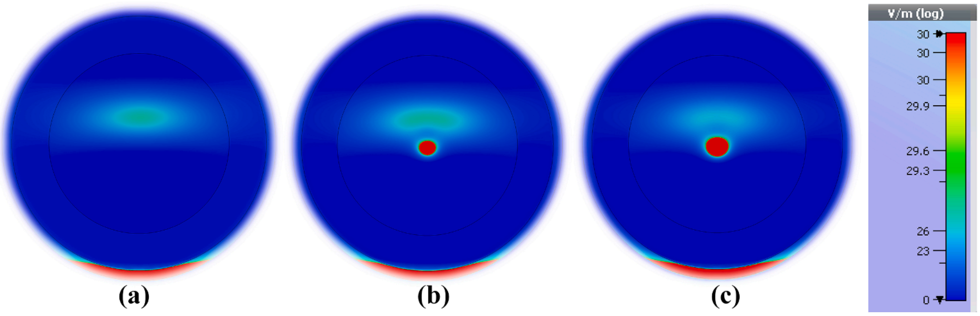

Fig. 26. MWI at 2.276 GHz, an E-field microwave imaging approach was used to evaluate tumor volume change: (a) normal; (b) fifth case; (c) sixth case.

Additionally, the sophisticated image reconstruction algorithms employed in MWI systems are adaptable and can be fine-tuned based on prior knowledge of expected electrical properties for different tissue types. This calibration during the reconstruction process enables the MWI system to accommodate the diverse anatomical layers present in breast and brain tissues, facilitating the accurate identification of potential anomalies.

The versatility of microwave imaging techniques, exemplified by advanced sensor systems like our microstrip patch antenna coupled with artificial magnetic conductor (AMC), enables the imaging of breast and brain tissues using a single applicator despite their anatomical differences. Our sensor's design incorporates features that account for the varying tissue compositions and layering within these organs, leading to precise and high-quality imaging for non-invasive cancer diagnosis. The presence of AMC in our antenna design enhances frequency selectivity, thereby improving the sensor's accuracy and sensitivity in detecting abnormalities. This enhancement, coupled with the directive radiation pattern of the antenna, contributes to high-accuracy imaging, making our sensor suitable for visualizing anomalies and facilitating early diagnosis and treatment planning in breast and brain cancer. Overall, our study underscores the adaptability and effectiveness of microwave imaging techniques in diverse medical applications, showcasing the potential of a unified applicator for imaging different anatomical regions.

The antenna is also suitable for tumor detection and microwave imaging of brain due to its performance discussed earlier. The brain model employed here has been shown in Fig. 27(a). It contains seven layers, and a high early detection pass rate. Fig. 27(b) shows four antennas in the arrangement for brain tumor detection. Multiple tumors show that cancer cells have grown and spread. The characteristics of these levels are shown in Table 3.

Table 3
Hemispheric head model's distinct tissues' electrical properties [26,27].

Tissue	Electric or Effective Conductivity (σ_{eff}) (S/m)	Relative Permittivity (ε_r)
Brain	1.29	43.22
Cerebrospinal fluid (CSF)	2.3	70.1
Dura	0.9	46
Bone (Skull)	0.03	5.6
Fat	0.04	5.54
Skin	0.73	45

As mentioned earlier, microwave imaging compares electrical properties of normal (healthy) cells and tissues to those of newly infected cancer cells or tumors. A pure brain phantom, an early-stage cancer with a 5 mm tumor radius, and an invasive cancer with many tumors constitute the three scenarios in which the sensor was employed. The second tumor had a smaller radius of 3 mm and was located 20 mm apart from the first. As seen in Fig. 28, tumors increase the concentration of the electric field, which helps in the detection and localization of tumors in the brain tissue. Our proposed sensor efficiently detects tumors by analyzing backscattering signals, and is a strong candidate for microwave brain imaging.

A detailed perpendicular examination of the tumor size was performed in six cases of early-stage brain cancer. The results revealed a substantial range in cancer sizes, from tiny, confined tumors to bigger, more invasive tumors. These results emphasize the significance of early identification and timely therapy in the management of brain cancer cases. The first instance featured a 1 mm-radius tumor, as shown in Fig. 29(b). A tumor with a radius of 2 mm is also shown in Fig. 29(c) in the second case.

As seen in Fig. 30(b), the third case showed a tumor with a 3 mm radius. In addition, Fig. 30(c) demonstrates that the fourth case revealed a tumor with a 4 mm radius. These results imply that the tumor sizes in the instances examined differed. It is significant to highlight that the tumor size was measured according to a standard procedure in order to guarantee precision and consistency in the patients' prognosis and available treatments. The variety in tumor size seen in this study emphasizes the significance of personalized treatment plans since tumors of various sizes may necessitate various therapies.

The fifth case's tumors had a 5 mm radius, as seen in Fig. 31(b). In addition, Fig. 31(c) demonstrates that the tumor in the sixth example had a radius of 6 mm. A substantial association between the sensor readings and the existence of the diagnostic condition was also found by the MWI method of analysis. Accordingly, it seems that the sensor shows a significant promise for precise diagnosis in clinical situations. Additionally, the sensor regularly outperforms other diagnostic techniques when compared with respect to accuracy and speed, making it a viable tool for future medical applications.

7. Benchmarking

Table 4 and Table 5 provide extensive comparison between the proposed antenna/sensor and recent state-of-the-art designs reported in the literature. The comparison is pertinent to antenna size, material parameters of the substrate, operating frequency range, and field properties (here, realized gain). As it can be observed, the proposed structure offers perhaps the best combination of the crucial performance parameters, specifically, the impedance matching bandwidth and gain, which are superior over those of the benchmark devices. It should also be recalled that the proposed structure exhibits an additional (low-frequency) resonance at about 2.3 GHz, which is associated with high gain, which improves MWI system resolution, thereby enabling early detection of even small tumors. Also, our antenna features small size, and it is cheap to manufacture due to being implemented on the FR4 material.

8. Conclusions

This article proposed a novel architecture of microstrip antenna and improved sensor for non-invasive (early-stage) breast cancer and brain cancer diagnosis. The antenna is based on a combination of microstrip patches and Vivaldi-like structure. In order to implement the sensor, the basic antenna is coupled with the AMC unit, realized on a separate substrate, and allocated at the 3 mm distance from the main radiator. The proposed arrangement is intended to improve the accuracy and sensitivity of microwave imaging by enhancing frequency selectivity and ensuring high gain. The presence of AMC results in an additional resonance allocated at the frequency of 2.276 GHz, which is associated with the broadside gain of 10 dBi. The improved selectivity achieved due to AMC gives the proposed antenna a competitive edge over the existing devices, which is indicative of its potential for usage in various

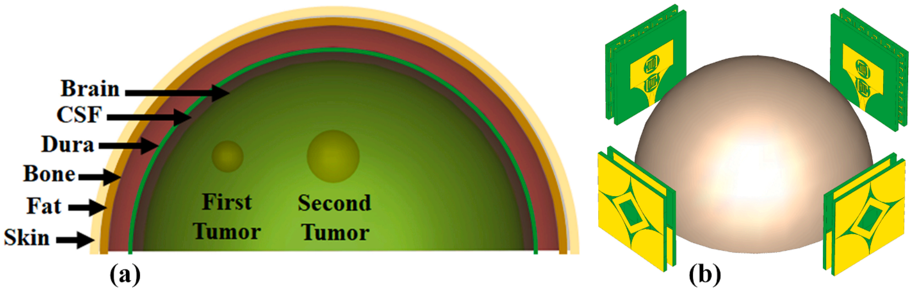

Fig. 27. Application of the proposed antenna for brain cancer detection: (a) cancerous brain phantom; (b) MWI system simulation setup.

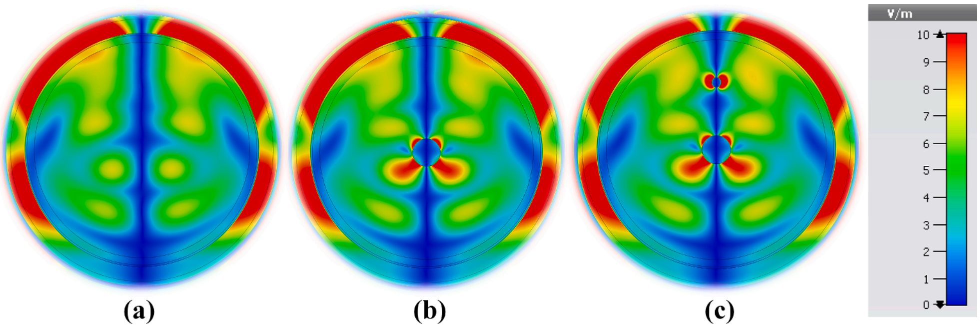

Fig. 28. E-field microwave imaging technique results at 2.276 GHz: (a) healthy brain; (b) early-stage brain cancer with one tumor; and (c) brain cancer with two tumors.

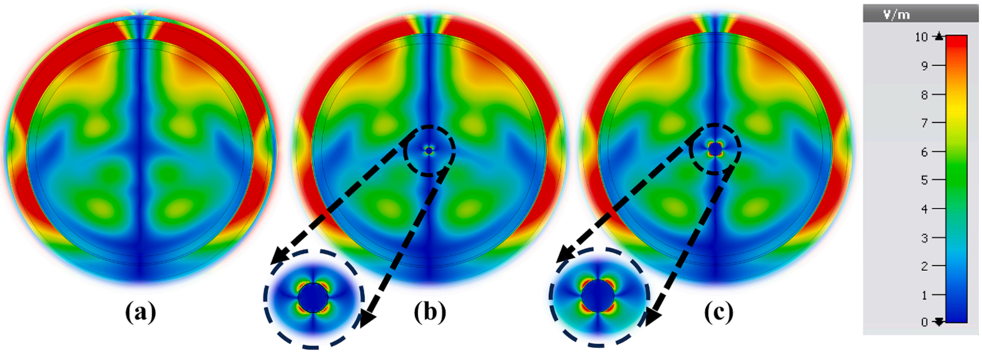

Fig. 29. E-field microwave imaging technique was utilized at 2.276 GHz to examine tumor volume change in: (a) a healthy brain; (b) the first case; and (c) the second case.

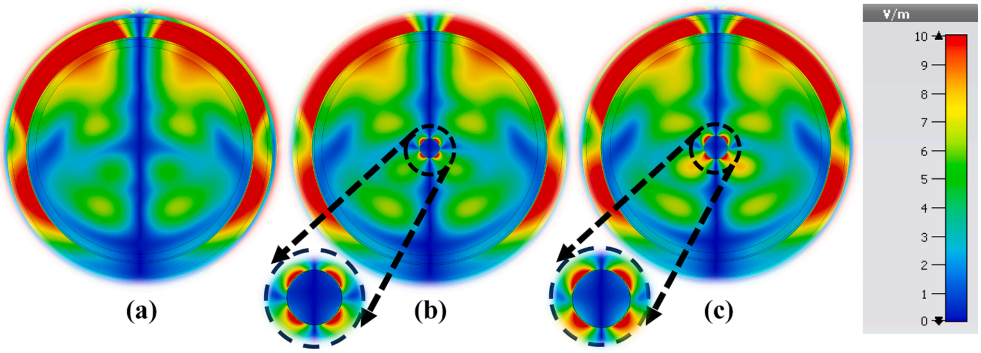

Fig. 30. E-field microwave imaging technique was utilized at 2.276 GHz to examine tumor volume change in: (a) a healthy brain; (b) third case; (c) fourth case.

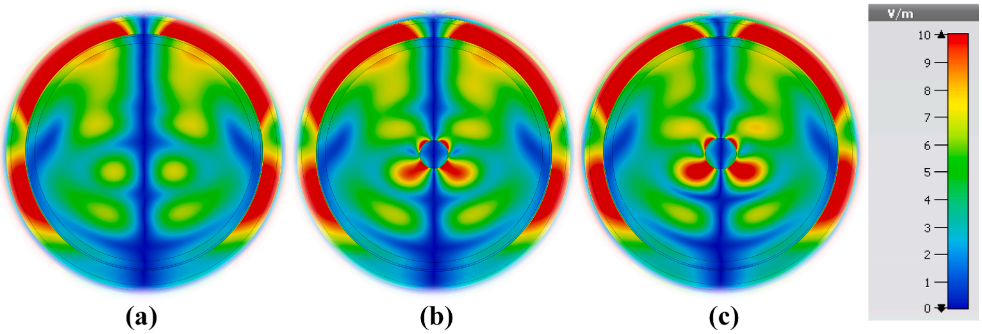

Fig. 31. E-field microwave imaging technique was utilized at 2.276 GHz to examine tumor volume change in: (a) a healthy brain; (b) fifth case; (c) sixth case.

Table 4
Comparison of suggested sensor for breast cancer detection with state-of-the-art antennas reported in the literature.

References	Structure Size (mm^2)	Substrate	Frequency Range (GHz)	Gain (dBi)	Year Published
[22]	40 × 40	FR4	3–11	7.06	2018
[12]	51 × 42	Rogers RT/duroid 5870	2–7.5	9.5	2019
[20]	21.44 × 23.53	FR4	3–12	5.76	2019
[21]	40 × 40	FR4	2–11	7.2	2019
[18]	40 × 40	FR4	2–11	7.2	2019
[8]	42 × 41	Rogers RT 5880	2–11	5.40	2020
[11]	20 × 19	FR4	2–12	5	2022
[7]	80 × 61	felt	4–15	7.56	2022
This work	35.6 × 35.6	FR4	2–14	11.7	–

Table 5
Comparison of suggested sensor for brain cancer detection with state-of-the-art antennas reported in the literature.

References	Structure Size (mm^2)	Substrate	Frequency Range (GHz)	Gain (dBi)	Year Published
[25]	70 × 15	Rogers 3003	0–3.5	3	2016
[34]	80 × 20	FR4	0.75–2.5	4.6	2016
[26]	31.68 × 31	Rogers R03003	3–10	6.77	2018
[28]	50 × 60	Rogers RO4350B	2–3	2.45	2019
[31]	59 × 59	Rogers R04003C	0.6–1.4	3.1	2019
[27]	50 × 44	Rogers RO4350B	1.5–4	5.65	2020
[29]	50 × 40	Rogers RT5880/ RO4350B	1.3–3.3	6.67	2022
This work	35.6 × 35.6	FR4	2–14	11.7	–

cancer diagnoses. Apart from high gain, the antenna exhibits directive radiation pattern, which ensures high accuracy and quality imaging in medical diagnostics, improving understanding, visualizing issues, and detecting anomalies for earlier diagnosis and better treatment options. To provide a better understanding of antenna operation, the electric and magnetic energy density, surface current distribution, and power have been investigated. The presented device has been fabricated and experimentally validated. EM simulation and measured results are in satisfactory agreement, including both electrical (reflection) and field performance figures (gain, E- and H-plane radiation patterns). The observed misalignments are minor, underscoring the relevance of the design procedure. The measured impedance matching follows EM-simulated predictions over a broad range of frequencies. The measured gain is as high as 11.7 dB at the resonant frequency of 2.279 GHz, which demonstrates the effects of incorporating AMC. The latter shows zero reflection phase at that frequency, which contributes to gain enhancement. The suitability of the presented sensor for real-world imaging applications that require high gain and directed radiation has been demonstrated by applying it in a MWI system. Multiple incidences of breast and brain cancer were identified for different forms of cancer, and various scenarios concerning the tumor size and spatial arrangements. The detection pass rate is as high as 95 %, when discriminating between healthy tissue and breast phantoms containing tumors. Also, the MWI system employing the proposed sensor can identify tumors of various sizes, even as small as 0.5 mm. Furthermore, our antenna has been favorably compared to state-of-the-art devices reported in the literature showing superiority in terms of operating bandwidth and gain, while maintaining small size.

Funding

This research was funded by the Ministry of Higher Education (MOHE), Malaysia through the Fundamental Research Grant Schemes (FRGS) under the grant number FRGS/1/2021/TK0/UKM/01/6 and the part of this research is supported by the Icelandic Research Fund Grant 2410297 and by National Science Centre of Poland Grant 2020/37/B/ST7/01448.

CRediT authorship contribution statement

Musa N. Hamza: Writing – original draft, Software, Resources, Formal analysis, Data curation, Conceptualization. **Mohammad Tariqul Islam:** Writing – review & editing, Software, Resources, Funding acquisition. **Slawomir Koziel:** Writing – review & editing, Writing – original draft, Supervision, Software, Resources, Funding acquisition, Data curation.

Declaration of Competing Interest

The authors declare that they have no known competing financial interests or personal relationships that could have appeared to influence the work reported in this paper.

Acknowledgements

This research was funded by the Ministry of Higher Education (MOHE), Malaysia through the Fundamental Research Grant Schemes (FRGS) under the grant number FRGS/1/2021/TK0/UKM/01/6 and the part of this research is supported by the Icelandic Research Fund Grant 2410297 and by National Science Centre of Poland Grant 2020/37/B/ST7/01448.

References

[1] A.G. Waks, E.P. Winer, Breast cancer treatment: A review, J. Am. Med. Assoc. 321 (2019) 288–300.
[2] N. Harbeck, F. Penault-Llorca, J. Cortes, M. Gnant, N. Houssami, P. Poortmans, K. Ruddy, J. Tsang, F. Cardoso, Breast cancer, *Nat. Rev. Dis. Primers* 5 (2019) 66.
[3] R. Siegal, K.D. Miller, A. Jemal, Cancer statistics, 2012, CA Cancer J. Clin. 64 (2014) 9–29.
[4] M.A. Aldhaeebi, K. Alzoubi, T.S. Almoneef, S.M. Bamatraf, H. Attia, M.R. O, Review of microwaves techniques for breast cancer detection. *Sensors (Basel)* (2020), 20.
[5] K. Shaikh, S. Krishnan, R.M. Thanki, Artificial Intelligence in Breast Cancer Early Detection and Diagnosis, Springer, 2021.
[6] M. Alibakhshikenari, B.S. Virdee, P. Shukla, N.O. Parchin, L. Azpilicueta, C.H. See, R.A. Abd-Alhameed, F. Falcone, I. Huynen, T.A. Denidni, E. Limiti, Metamaterial-Inspired antenna array for application in microwave breast imaging systems for tumor detection, IEEE Access 8 (2020) 174667–174678.
[7] K. Hossain, T. Sabapathy, M. Jusoh, S.H. Lee, K.S.A. Rahman, M.R. Kamarudin, Negative index metamaterial-based frequency-reconfigurable textile CPW Antenna for microwave imaging of breast cancer, Sensors (Basel) (2022) 22.
[8] A. Hossain, M.T. Islam, M.T. Islam, M.E.H. Chowdhury, H. Rmili, M. Samsuzzaman, A Planar ultrawideband patch antenna array for microwave breast tumor detection, Materials (Basel) (2020) 13.
[9] M.Z. Mahmud, M.T. Islam, N. Misran, S. Kibria, M. Samsuzzaman, Microwave Imaging for breast tumor detection using uniplanar AMC based CPW-Fed microstrip antenna, IEEE Access 6 (2018) 44763–44775.
[10] P.K. Rao, A.R. Yadav, R. Mishra, AMC-based antenna sensor for breast tumors detection, Int. J. Microw. Wirel. Technol. 13 (2020) 954–961.
[11] F.E. Zerrad, M. Taouzari, E.M. Makroum, J. El Aoufi, M.T. Islam, V. Ozkaner, Y. I. Abdulkarim, M. Karaaslan, Multilayered metamaterials array antenna based on artificial magnetic conductor's structure for the application diagnostic breast cancer detection with microwave imaging, Med. Eng. Phys. 99 (2022) 103737.
[12] M.T. Islam, M.Z. Mahmud, M.T. Islam, S. Kibria, M. Samsuzzaman, A low cost and portable microwave imaging system for breast tumor detection using UWB directional antenna array, Sci. Rep. 9 (2019) 15491.
[13] E.C. Fear, X. Li, S.C. Hagness, M.A. Stuchly, Confocal microwave imaging for breast cancer detection: Localization of tumors in three dimensions, IEEE Trans. Biomed. Eng. 49 (2002) 812–822.

[14] E. Fear, A. Low, J. Sill, M.A. Stuchly, Microwave system for breast tumor detection: Experimental concept evaluation, in: IEEE Antennas and Propagation Society International Symposium (IEEE Cat No 02CH37313), IEEE, 2002, pp. 819–822.

[15] D. Li, P.M. Meaney, K.D. Paulsen, Conformal microwave imaging for breast cancer detection, IEEE Trans. Microw. Theory Tech. 51 (2003) 1179–1186.

[16] Y. Cheng, M. Fu, Dielectric properties for non-invasive detection of normal, benign, and malignant breast tissues using microwave theories, Thorac Cancer 9 (2018) 459–465.

[17] M.T. Islam, M. Samsuzzaman, M.T. Islam, S. Kibria, M.J. Singh, A homogeneous breast phantom measurement system with an improved modified microwave imaging antenna sensor, Sensors (Basel) (2018) 18.

[18] M. Samsuzzaman, M.T. Islam, M.T. Islam, A.A.S. Shovon, R.I. Faruque, N. Misran, A 16-modified antipodal Vivaldi antenna array for microwave-based breast tumor imaging applications, Microw. Opt. Technol. Lett. 61 (2019) 2110–2118.

[19] N. Misran, S.H. Yusop, M.T. Islam, M.Y. Ismail, Analysis of parameterization substrate thickness and permittivity for concentric split ring square reflectarray element, Jurnal Kejuruteraan (J. Eng.) 23 (2012) 11–16.

[20] M.T. Islam, M. Samsuzzaman, M. Faruque, M.J. Singh, M. Islam, Microwave imaging based breast tumor detection using compact wide slotted UWB patch antenna, Optoelectron. Adv. Mater. Rapid Commun. 13 (2019) 448–457.

[21] S. Kibria, M. Samsuzzaman, M.T. Islam, M.Z. Mahmud, N. Misran, M.T. Islam, Breast phantom imaging using iteratively corrected coherence factor delay and sum, IEEE Access 7 (2019) 40822–40832.

[22] M.T. Islam, M. Samsuzzaman, M.T. Islam, S. Kibria, M.J. Singh, A homogeneous breast phantom measurement system with an improved modified microwave imaging antenna sensor, Sensors 18 (2018) 2962.

[23] M.T. Islam, M.Z. Mahmud, N. Misran, J.-I. Takada, M. Cho, Microwave breast phantom measurement system with compact side slotted directional antenna, IEEE Access 5 (2017) 5321–5330.

[24] E. Porter, H. Bahrami, A. Santorelli, B. Gosselin, L.A. Rusch, M. Popović, A wearable microwave antenna array for time-domain breast tumor screening, IEEE Trans. Med. Imaging 35 (2016) 1501–1509.

[25] A.T. Mobashsher, K.S. Bialkowski, A.M. Abbosh, Design of compact cross-fed three-dimensional slot-loaded antenna and its application in wideband head imaging system, IEEE Antennas Wirel. Propag. Lett. 15 (2016) 1856–1860.

[26] R. Inum, M.M. Rana, K.N. Shushama, M.A. Quader, EBG based microstrip patch antenna for brain tumor detection via scattering parameters in microwave imaging system, Int. J. Biomed. Imaging 2018 (2018).

[27] A. Hossain, M.T. Islam, M.E. Chowdhury, M. Samsuzzaman, A grounded coplanar waveguide-based slotted inverted delta-shaped wideband antenna for microwave head imaging, IEEE Access 8 (2020) 185698–185724.

[28] A. Salleh, C.C. Yang, M.S.J. Singh, M.T. Islam, Development of antipodal Vivaldi antenna for microwave brain stroke imaging system, Int. J. Eng. Technol. 8 (2019) 162–168.

[29] A. Hossain, M.T. Islam, G.K. Beng, S.B.A. Kashem, M.S. Soliman, N. Misran, M. E. Chowdhury, Microwave brain imaging system to detect brain tumor using metamaterial loaded stacked antenna array, Sci. Rep. 12 (2022) 16478.

[30] A.S. Alqadami, N. Nguyen-Trong, B. Mohammed, A.E. Stancombe, M. T. Heitzmann, A. Abbosh, Compact unidirectional conformal antenna based on flexible high-permittivity custom-made substrate for wearable wideband electromagnetic head imaging system, IEEE Trans. Antennas Propag. 68 (2019) 183–194.

[31] I. Merunka, A. Massa, D. Vrba, O. Fiser, M. Salucci, J. Vrba, Microwave tomography system for methodical testing of human brain stroke detection approaches, Int. J. Antennas Propag. 2019 (2019).

[32] J.A. Tobon Vasquez, R. Scapaticci, G. Turvani, G. Bellizzi, N. Joachimowicz, B. Duchêne, E. Tedeschi, M.R. Casu, L. Crocco, F. Vipiana, Design and experimental assessment of a 2D microwave imaging system for brain stroke monitoring, Int. J. Antennas Propag. 2019 (2019) 1–12.

[33] M. Rokunuzzaman, A. Ahmed, T.C. Baum, W.S. Rowe, Compact 3-D antenna for medical diagnosis of the human head, IEEE Trans. Antennas Propag. 67 (2019) 5093–5103.

[34] A. Mobashsher, A. Abbosh, Compact 3-D slot-loaded folded dipole antenna with unidirectional radiation and low impulse distortion for head imaging applications, IEEE Trans. Antennas Propag. 64 (2016) 3245–3250.

[35] A.S. Alqadami, K.S. Bialkowski, A.T. Mobashsher, A.M. Abbosh, Wearable electromagnetic head imaging system using flexible wideband antenna array based on polymer technology for brain stroke diagnosis, IEEE Trans. Biomed. Circuits Syst. 13 (2018) 124–134.

[36] W. Wang, Z. Fang, K. Tang, X. Wang, Z. Shu, Z. Zhao, Y. Zheng, Wideband gain enhancement of MIMO antenna and its application in FMCW radar sensor integrated with CMOS-based transceiver chip for human respiratory monitoring, IEEE Trans. Antennas Propag. 71 (2022) 318–329.

[37] W. Wang, Y. Zheng, Wideband gain enhancement of high-isolation Fabry-Pérot antenna array with tandem circular parasitic patches and radial gradient PRS, IEEE Trans. Antennas Propag. 69 (2021) 7959–7964.

[38] W. Wang, S. Yang, Z. Fang, Q. Sun, Y. Chen, Y. Zheng, Compact dual-polarized wideband antenna with dual-/single-band shifting for microbase station applications, IEEE Trans. Antennas Propag. 69 (2021) 7323–7332.

[39] W. Wang, Q. Cao, Y. Zheng, Bandstop frequency-selective structures based on stepped-impedance loop resonators: Design, analysis, and measurement, IEEE Trans. Antennas Propag. 67 (2018) 1053–1064.

[40] W. Wang, Y. Zheng, Wideband gain enhancement of a dual-polarized MIMO vehicular antenna, IEEE Trans. Veh. Technol. 70 (2021) 7897–7907.

[41] W. Wang, Z. Zhao, Q. Sun, X. Liao, Z. Fang, K.Y. See, Y. Zheng, Compact quad-element vertically-polarized high-isolation wideband MIMO antenna for vehicular base station, IEEE Trans. Veh. Technol. 69 (2020) 10000–10008.

[42] W. Wang, Z. Qu, Z. Zheng, K.S.Y. Phua, C. Ivan, K.Y. See, Y. Zheng, Analysis and design of coil-based electromagnetic-induced thermoacoustic for rail internal-flaw inspection, IEEE Trans. Intell. Transp. Syst. 20 (2018) 2691–2702.

[43] M. Najumunnisa, A.S.C. Sastry, B.T.P. Madhav, S. Das, N. Hussain, S.S. Ali, M. Aslam, A metamaterial inspired AMC backed dual band antenna for ISM and RFID applications, Sensors 22 (2022) 8065.

[44] T.J. Cui, D.R. Smith, R. Liu, Metamaterials, Springer, 2010.

[45] R.E. Collin, Field Theory of Guided Waves, John Wiley & Sons, 1990.

[46] A. Ghosh, V. Kumar, G. Sen, S. Das, Gain enhancement of triple-band patch antenna by using triple-band artificial magnetic conductor, IET Microwaves Antennas Propag. 12 (2018) 1400–1406.

[47] M. Mahmud, S. Kibria, M. Samsuzzaman, N. Misran, M. Islam, A new high performance hibiscus petal pattern monopole antenna for UWB applications, Appl. Comput. Electromagn. Soc. J. (ACES) (2016) 373–380.

[48] A. Langtry, Understanding Cancer of the Breast, Irish Cancer Society, Dublin, Ireland, 2008.

[49] P.T. Nguyen, A.M. Abbosh, S. Crozier, Thermo-dielectric breast phantom for experimental studies of microwave hyperthermia, IEEE Antennas Wirel. Propag. Lett. 15 (2016) 476–479.